International Journal of Pharmaceutics 695 (2026) 126808

Contents lists available at ScienceDirect

International Journal of Pharmaceutics

journal homepage: www.elsevier.com/locate/ijpharm

Co-encapsulated fluorescent magnetic nanoparticles for potential applications in breast cancer therapy: Exploratory *in vitro* and in vivo studies

Stefan Sandu [a,b], Gianina Dodi [a], Ioannis Gardikiotis [a], Bianca-Elena-Beatrice Cretu [a,c], Andreea Luca [a], Florina Daniela Cojocaru [a], Liliana Verestiuc [a], Sorin-Aurelian Pasca [d], Vera Balan [a,*]

[a] Grigore T. Popa University of Medicine and Pharmacy Iasi, 16 University Street, 700115 Iasi, Romania
[b] Universite Lille, CNRS, Universite Polytechnique Hauts-de-France, UMR 8520 – IEMN - Institut d'Electronique de Microélectronique et de Nanotechnologie, F-59000 Lille, France
[c] Petru Poni Institute of Macromolecular Chemistry, Natural Polymers, Bioactive and Biocompatible Materials, Grigore Ghica Voda Alley 41A, 700487 Iasi, Romania
[d] Ion Ionescu de la Brad University of Life Sciences, Faculty of Veterinary Medicine, Department of Pathology, 8 M. Sadoveanu Alley, 700489 Iasi, Romania

ARTICLE INFO

Keywords:
Co-encapsulated
Magnetic nanoparticles
Docetaxel
Verapamil
MCF-7 spheroids
in vitro
in vivo toxicity

ABSTRACT

This study describes, for the first time in the literature, a suitable approach to develop co-encapsulated magnetic nanoparticles based on fluorescent biotinylated N-palmitoyl chitosan, hydrophobic magnetite, Docetaxel and Verapamil. The multicomponent nanostructures were obtained using a two-step method: ultrasonication-induced self-assembly followed by ionic gelation. Structural composition was confirmed by infrared spectroscopy; the magnetic nanostructures displayed an average hydrodynamic diameter of 322.20 ± 2.50 nm, a positive surface charge (5.63 ± 0.16 mV), good magnetic saturation (13.35 emu/g) and superparamagnetic behavior. *In vitro* drug release studies revealed a pH-responsive behavior for both encapsulated agents, with an enhanced release of the Verapamil. Cytotoxicity evaluation using live/dead assays on MCF-7 tumor spheroids embedded in collagen-based hydrogels demonstrated a substantial therapeutic effect. Serum interleukin-8 (IL-8) levels were quantified to evaluate systemic inflammatory responses following intravenous administration of drug free magnetic nanoparticles. IL-8 concentrations were considerably increased at day 3, indicating an acute inflammatory response, decreased during the subacute phase (days 7 and 14) and returned to control levels by day 21, demonstrating good biocompatibility. No significant toxicity was observed for magnetic nanoparticles in the rats. Overall, these findings suggest that the developed magnetic nanoplatforms represents a promising candidate for breast cancer applications and merits further *in vivo* investigation to elucidate the action mechanism of encapsulated therapeutics and their pharmacologic activity.

1. Introduction

Although promising, current breast cancer therapies (e.g surgery, chemotherapy or radiotherapy) are still limited due to the lack of selectivity, multidrug resistance (MDR) and various severe side effects (Aravindan et al., 2024; Lepeltier et al., 2020; Barzaman et al., 2020). Chemotherapeutic agents like Docetaxel, Cyclophosphamide, Fluorouracil, Doxorubicin hydrochloride and Methotrexate are used as the main treatment in breast cancer management, either alone or in combination (Park et al., 2017). Currently available commercial formulations of Docetaxel represent effective therapeutic approach of metastatic breast cancer and early-stage breast cancer (Panthi et al., 2023; Lu et al., 2016) but induce serious side effects such as neutropenia, hypersensitivity reactions, peripheral neuropathy and musculoskeletal toxicity (Imran et al., 2020). In addition, their poor aqueous solubility (Da Silva et al., 2018) and MDR largely limits their clinical applications, as these

* Corresponding author at: Faculty of Medical Bioengineering, Grigore T. Popa University of Medicine and Pharmacy Iasi, Mihail Kogalniceanu Street, 700454, Romania.
E-mail addresses: stefan.sandu@univ-lille.fr (S. Sandu), gianina.dodi@umfiasi.ro (G. Dodi), dr.gardikiotis@yahoo.com (I. Gardikiotis), cretu.bianca@icmpp.ro (B.-E.-B. Cretu), andreea.luca@umfiasi.ro (A. Luca), florina.cojocaru@umfiasi.ro (F.D. Cojocaru), liliana.verestiuc@bioinginerie.ro (L. Verestiuc), sorin.pasca@iuls.ro (S.-A. Pasca), balan.vera@umfiasi.ro (V. Balan).

https://doi.org/10.1016/j.ijpharm.2026.126808
Received 11 February 2026; Received in revised form 19 March 2026; Accepted 20 March 2026
Available online 25 March 2026

drugs can be expelled from cells by P-glycoprotein (P-gp) and consequently reduce their therapeutic effect, that often results in tumour recurrence, metastasis and death.

Combined chemotherapy was proposed to be used as a viable solution to overcome the MDR, namely co-administration of two or more pharmaceuticals using a multifunctional nanoplatform (Cheng, 2019), to capitalize on potential synergistic effects of drugs, along with active tumour targeting, improved uptake and reduced off-target effects (Tang et al., 2020).

Several agents, such as Verapamil, Cyclosporin A, Tamoxifen and calmodulin antagonists are recommended to modulate the P-gp transporter activity (Avendano and Menéndez, 2002). Among them, Verapamil, a calcium channel antagonist, is the first drug clinically attested for MDR reversal (Wang, 2011), being able to completely reverse *in vitro* drug resistance aroused from P-gp (Holohan, 2013), and extend the antitumoral effect of Docetaxel (Guo et al., 2017; Das et al., 2021).

In the last years, extensive research was focused in developing tumour-specific therapies, particularly employing multifunctional magnetic nanostructures (Gote et al., 2021; Liu et al., 2024; Payamifar et al., 2025), co-loaded with two therapeutic agents as an efficient strategy in breast cancer management. Current state-of-the-art systems are primarily based on superparamagnetic iron oxide nanoparticles engineered with biocompatible coatings (e.g., polymers, liposomes, silica, or biomimetic shells) to enable high drug loading, stability, and controlled release (Pareek et al., 2025; Graham et al., 2025; Yang et al., 2025). Dual-drug platforms typically combine two chemotherapeutics or integrate chemotherapy with gene therapy (e.g., siRNA), photothermal therapy, or magnetic hyperthermia to achieve synergistic antitumor effects (Ashrafizadeh et al., 2023; Tan et al., 2023). Advanced designs incorporate stimuli-responsive linkers (pH, redox, enzyme, or magnetic field-triggered) to ensure site-specific drug release within the tumour microenvironment. Towards the same goal, many platforms are developed as theranostic agents, combining drug delivery with imaging capabilities (e.g., MRI contrast enhancement), thereby enabling real-time treatment monitoring (Mi, 2020; Demiral et al., 2022; Cui et al., 2022).

Most of the reported studies demonstrated at preclinical level, improved cellular internalization, enhanced cytotoxic synergy, and the potential to overcome MDR; however, significant challenges remain and are related to long-term biosafety, large-scale reproducibility, pharmacokinetics, and clinical translation. In this framework, co-integration of MDR-reversal agents, like Verapamil, and chemotherapeutic agents, such as Docetaxel into functionalized magnetic nanoparticles could represent an active frontier for targeted breast cancer approaches.

Indeed, versatile magnetic nanosystems can encapsulate two or more pharmaceuticals, with the aim to achieve a synergistic effect, and offer significant advantages, namely targeting of multiple signalling pathways of cells (Rahmanian et al., 2021), increasing the drugs efficiency, and preventing also the side effects (Su et al., 2021; Tian et al., 2018).

The primary focus in assessing their impact as alternative strategies in cancer treatment relies in defining their physicochemical characteristics and biological behaviour (Pareek et al., 2025; Nivethaa et al., 2025). To enhance their biocompatibility or to precisely modulate toxic selectivity mechanisms, different functionalization strategies, employing natural and synthetic polymers, conjugated with biologically active molecules (e.g., vitamins, antibodies) were investigated (Ursachi et al., 2023).

Among polymers, chitosan emerges as a highly effective polysaccharide endowed with advantageous properties and extensively employed in the development of magnetic nanostructures for biomedical applications (Wang et al., 2020). This has consequently stimulated the design of tailored formulations based on novel biofunctionalized chitosan derivatives (Jaiswal et al., 2021; Guo et al., 2024). In agreement with worldwide researchers' efforts, our group synthesized a biofunctionalized polymer, namely biotinylated N-palmitoyl chitosan and exploited its potential to combine the targeting ability of biotin, with the outstanding features of amphiphilic chitosan, especially for drug delivery applications (Balan et al., 2021; Balan et al., 2016). In a previous study, we proposed a straightforward strategy to design Docetaxel self-assembled nanoparticles with good drug loading, a pH-dependent release profile, hemocompatibility and susceptibility to biodegradation (Balan et al., 2016). In a further report, we extended these nanostructures by entrapment of magnetite. The obtained magnetic platform demonstrated sustained drug release and pronounced cytotoxic activity against breast cancer cell lines (Serban et al., 2023).

Drawing on these encouraging results, this paper proposes a simple method to develop co-encapsulated magnetic nanoparticles based on fluorescent biotinylated N-palmitoyl chitosan, magnetite, Docetaxel and Verapamil and assess their physico-chemical and biological characteristics. To our best knowledge, no other multifunctional platform that combines all these components was described in the literature.

2. Materials and methods

2.1. Materials

Biotin functionalized N-palmitoyl chitosan (**BPCs**; Number-average molecular weight, determined by gel permeation chromatography; Mn – 238.50 kDa; biotinylation degree –quantified by 4-hydroxyazobenzene-2-carboxylic acid (HABA)/avidin assay- 0.34 nmol/mg polymer) and hydrophobic magnetite double coated with sodium oleate (**Mag-NaOl**) were prepared, according to our previously published methods (Balan et al., 2016; Dodi et al., 2015). The other chemical compounds, namely: Sodium tripolyphosphate (**TPP**), Docetaxel (**DCX**), Verapamil (**VER**), Fluorescein isothiocyanate, (**FITC**) and solvents (acetic acid and ethanol) were purchased from Sigma-Aldrich. The MCF-7 (human Caucasian breast adenocarcinoma cell line) were acquired from the European Collection of Cell Cultures (ECACC).

2.2. Synthesis of fluorescent biotinylated N-palmitoyl chitosan (BPCs-FITC)

The fluorescent marker (FITC) was attached on the biotinylated N-palmitoyl chitosan, as depicted in Fig. 1A. To the BPCs solution (100 mL, 10 mg/mL in 0.1 M aqueous acetic acid) 25 mL of FITC (2 mg/mL) were added and continuously stirred for 3 hours (h), in the dark. Then, the fluorescent biotinylated polymer was precipitated with an alkaline solution (NaOH, 0.5 M), purified with double distilled water, until no fluorescence was detected in the supernatant, freeze-dried and further analysed by FT-IR Spectroscopy (Fig. 2).

2.3. Synthesis of co-encapsulated magnetic nanoparticles

Co-encapsulated magnetic nanoparticles were prepared by self-assembly of fluorescent BPCs, in the presence of hydrophobic magnetite (Mag-NaOl), and the drugs (DCX and VER) followed by ionic gelation (Fig. 1B), as described below. First, DCX (1 mL, 1 mg/mL in ethanol) was added to a suspension of Mag-NaOl (10 mL, 0.5%) (Fig. 1B.I); then VER (1 mL, 1 mg/mL in ethanol) was added to 50 mL of BPCs (0.2% in 0.1 M acetic acid) (Fig. 1B.II) and subsequently combined, under mechanical stirring (700 rpm, 30 min) (Fig. 1B.III). Lately, the mixture was subjected to ultrasonication (Bandelin Ultrasonic Homogenizer, 200 W output, continuous pulse, 100% amplitude, 1 min) (Fig. 1B.IV; self-assembly phase). After a dropwise addition of aqueous TPP (9 mL, 0.2%), the mixture was mechanically stirred for another 2 h (Fig. 1B.V-ionic gelation phase). Finally, the co-encapsulated magnetic nanoparticles **(NP-DCX-VER)** were collected by centrifugation (10000 rpm), purified by centrifugation/redispersion cycles in double distilled water and freeze dried. Magnetic nanoparticles without drug (**NPs)** were also prepared, and their toxicity in small animals was evaluated (Section 2.8 and 3.5).

Table 1
Korsmeyer-Peppas model interpretation for polymeric matrices with spherical geometry.

Diffusional exponent (n)	Drug release mechanism
$n \leq 0.43$	Fickian diffusion
$0.43 < n < 0.85$	Anomalous transport
$n = 0.85$	Case-II transport
$n > 0.85$	Super case-II transport

2.4. Characterization of magnetic nanoparticles

A Vertex 70 (Bruker) FT-IR spectrophotometer was used to record the spectra of all samples (resolution of 4 cm^{-1}, 400–4000 cm^{-1}). The morphology of the magnetic nanoparticles was investigated by transmission electron microscopy (TEM) using a dried sample (FEI Tecnai F20 field-emission high-resolution transmission electron microscope operated at an accelerating voltage of 200 kV and equipped with an Eagle 4 k CCD camera). Zeta potential and hydrodynamic mean diameter of magnetic nanoparticles in liquid state were determined by dynamic light scattering (DLS) measurements performed in water and plasma simulated fluid (pH = 7.4) at 25°C, using a Malvern ZetasizerNanoS (Malvern Instruments, UK), following a suitable dilution. The samples were ultrasonicated for 3 minutes (min.) and then equilibrated at 25°C prior to size and zeta-potential measurements for 5 min. Particles magnetization was measured at 25°C (Lakeshore 7400 vibrating sample magnetometer system, ±10000 G applied magnetic field).

2.5. In vitro drug release studies

Drug loading for DCX and VER was calculated according to (Eq.1); where W_{added} and W_{free} are the amount of DCX/VER initially added, and respectively the amount of free DCX/VER in the supernatant (after nanoparticles separation by centrifugation), and quantified by UV–Vis Spectroscopy (UV-1700 PharmaSpec, Shimadzu) at 229 nm for DCX and 278 nm for VER, whereas $W_{MN\_DCX\_VER}$ is the weight of magnetic nanoparticles.

$$DL\,(\%) = \left(W_{added\_} W_{free}\right)/W_{MN\_DCX\_VER} \times 100 \quad (1)$$

In vitro release profiles were studied in two PBS media (pH 7.4 and 5.5), in an incubator shaker, at 37°C. Briefly, 1 mL of NP-DCX-VER suspension was added into a dialysis bag (molecular weight cut-off 12400 Da) and placed in 22 mL PBS. At time intervals, 1.5 mL outside solution was removed, for analysis by UV–Vis Spectroscopy, at 229 nm and 278 nm, (UV-1700 PharmaSpec, Shimadzu, n = 3), and subsequently replaced with fresh media.

DOX and VER release mechanisms were studied by fitting the dissolution data (the first 72 h) into four kinetic models: zero-order, first-order, Higuchi, and Korsmeyer-Peppas (t = 0 was not included) (Arısoy and Comoglu, 2020). Zero-order model is expressed as the cumulative amount of drug released *versus* time (Eq. (2)) and describes a constant drug release from pharmaceutical forms, independent of the drug concentration (Wojcik-Pastuszka et al., 2019).

$$Q_t = Q_0 + k_0 t \quad (2)$$

First-order model is reported in terms of the log cumulative amount of drug remaining *versus* time (Eq. (3)) and explains the drug release pattern when the rate is dependent on the drug concentration (Sanchez-Orozco et al., 2023).

$$LogQ_t = LogQ_0 - k_0 t/2.303 \quad (3)$$

Higuchi model is obtained by plotting the cumulative amount of drug released *versus* square root (SQRT) of time (Eq. (4)) and acknowledge a drug release from the matrix as a diffusion process based on Fick's law (Paarakh et al., 2018).

$$Q_t = k_H t^{1/2} \quad (4)$$

Korsmeyer-Peppas model is expressed as the log cumulative amount of drug released *versus* log of time (Eq. (5)) and evaluates a drug release pattern from a polymeric system (Korsmeyer et al., 1983; Heredia et al., 2022).

$$Q_t/Q_\infty = k\ t^n Q_t/Q_0\ \ k \quad (5)$$

Q_t is the amount of drug released at time t; Q_0 represents the initial amount of drug in the solution; k defines kinetic constant for each model, Q_t/Q_∞ describes the fraction of drug released, and n the diffusional release exponent indicating the drug release mechanism (Table 1). The k, n, residual sum of squares (**RSS**), and correlation coefficient ($\mathbf{R^2}$) values were calculated using regression analysis of the plots.

2.6. In vitro cytotoxicity. Live/Dead assay in MCF-7 spheroids

Live/Dead cell double staining kit (Sigma Aldrich) was used to analyse the cytotoxicity of NP-DCX-VER on MCF-7 spheroids, by fluorescence microscopy (Leica DMI3000 microscope). The spheroids were obtained by encapsulation of MCF-7 cells ($2x10^5$) in oxidized hyaluronic acid crosslinked collagen hydrogels, as previously described (Luca et al, 2021). The cell suspensions in the hydrogel mixtures were incubated at 37°C, 6 days. At day 6, when the spheroids were formed, magnetic nanoparticles (30 μg/mL) were added and cytotoxicity was evaluated, against control spheroids encapsulated in similar conditions, after 24, 48, 72 h and 8 days.

2.7. In vivo toxicity evaluation

2.7.1. Animals

Female Wistar rats (healthy, 16 weeks old; weighing between 254 ± 15 g; 8 animals/group) were housed in temperature and humidity-controlled individually ventilated cages (12:12-h light–dark cycle) with free access to water and a standard pellet diet. All procedures were approved by the Ethical Committee of the Grigore T. Popa University of Medicine and Pharmacy of Iasi (no. 17/25.10.2020), authorised by the National Sanitary Veterinary and Food Safety Authority (no. 51/18.03.2022) and followed the EU Directive 2010/63 for animals' experiments. The number of animals in each group follows the reduction principles of the 3Rs.

2.7.2. Intravenous toxicity test

The animals were randomly divided into experimental and control groups (study design). The animals received either magnetic nanoparticles (NPs) by single intravenous injection for the experimental group or saline solution (NaCl 0.9%) for the control group. Before injection, the animals from each batch were anesthetized by inhalation with isoflurane gas (Isoflutek 1000 mg/g, Laboratorios Karizoo, Spain) mixed with normal air (5% for induction and 2% maintenance). Their tail skin was cleaned with 70% alcohol solution. A suspension of the NPs (100 μL, 2 mg/mL) was homogenized in saline solution by ultrasound irradiation (30 s with 45 W nominal output, in continuous pulse and 100% amplitude) and injected slowly, through the tail vein at a dose of 0.71 mg/kg (intravenous (*iv*) administration). The injected NP volume was 250 μL, with individual injection volumes adjusted on animal weight. Animals were allowed to recover following nanoparticles injection and then returned to their cages. After administration, all animals were continuously observed for clinical signs of toxicity and possible mortality during the first four hours and every day for 21 days. Their weight was determined at 0, 3, 7, 14 and 21 days after nanoparticles injection. Results were expressed as mean ± standard deviation. No animals or data were excluded from the experiment.

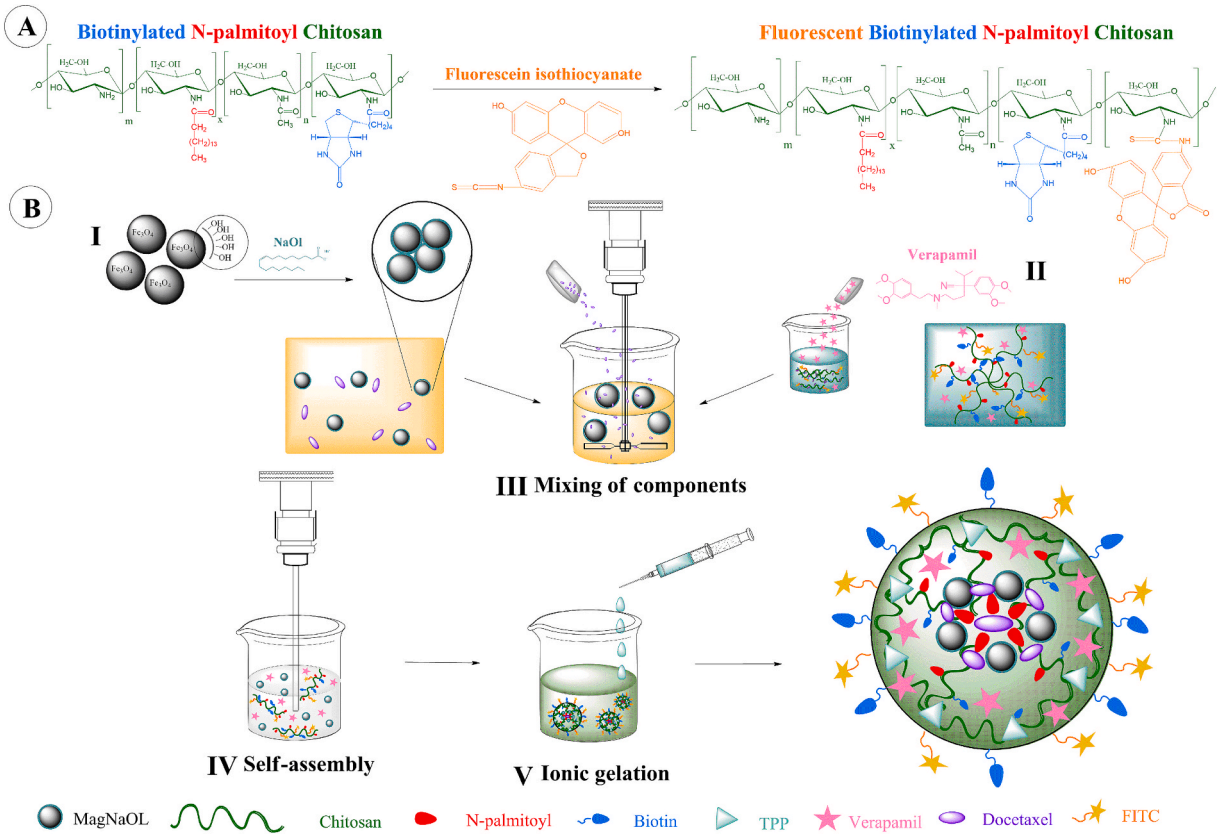

Fig. 1. (A) Schematic representation of fluorescent biotinylated N-palmitoyl chitosan synthesis and (B) co-encapsulated magnetic nanoparticles **(NP-DCX-VER)** preparation steps.

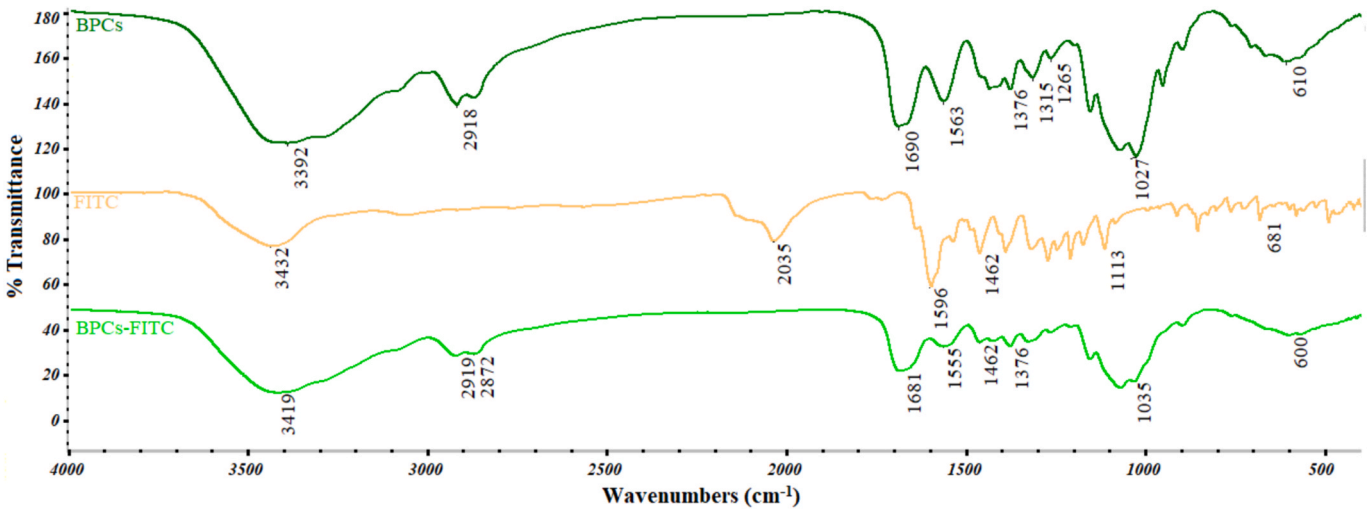

Fig. 2. FT-IR spectra of biotinylated polymer (BPCs), fluorescent marker (FITC), and fluorescent biotinylated polymer (BPCs-FITC).

2.7.3. Enzyme-linked immunosorbent assay (ELISA)

Blood samples were collected before the injection (day 0), and at, 3, 7, 14 and 21 days after the injection, to determine the serum level of interleukin (IL)-8 using a commercially available ELISA kit (code ABIN6968034, Antibodies-online GmbH, Aachen, Germany) according to the manufacturer's recommendation. Shortly, 100 μL of standards, blank, and samples (diluted 1:1 with buffer) were added into wells and incubated at 37°C for 90 min (plate incubator Matrix Orbital Delta plus IKA, Staufen, Germany), followed by addition of 100 μL biotin-labeled antibody and incubation at 37°C for another 60 min. Next, 100 μL of HRP-streptavidin conjugate were added, incubated at 37°C for 30 min, washed, and after that 3,3′,5,5′-tetramethylbenzidine (TMB) substrate solution (90 μL) was pipetted into the plate and kept at 37°C for 30 min. Finally, 50 μL of stop solution was added to each well, and the optical density was determined at 450 nm using the Tecan Sunrise Plate Reader, Switzerland. All measurements were performed in triplicate. MyAssays software (MyAssays Ltd, Brighton, East Sussex, UK) was used to analyse all samples. The levels of IL-8 were calculated using the standard curve and expressed as pg/mL.

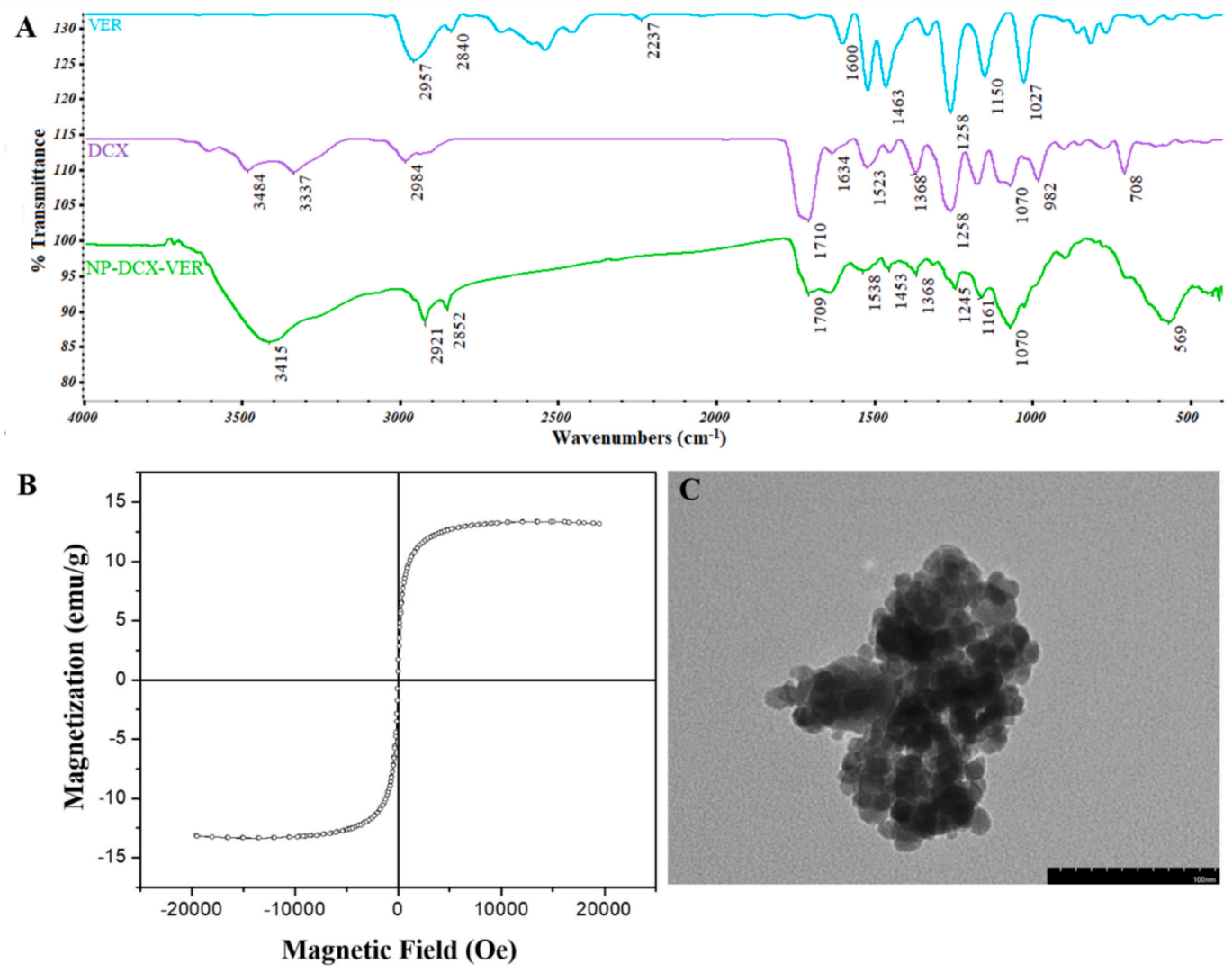

Fig. 3. FT-IR spectra of VER, DCX and NP-DCX-VER (A); Magnetization curve (B) and TEM image of NP-DCX-VER (C, scale bar 100 nm).

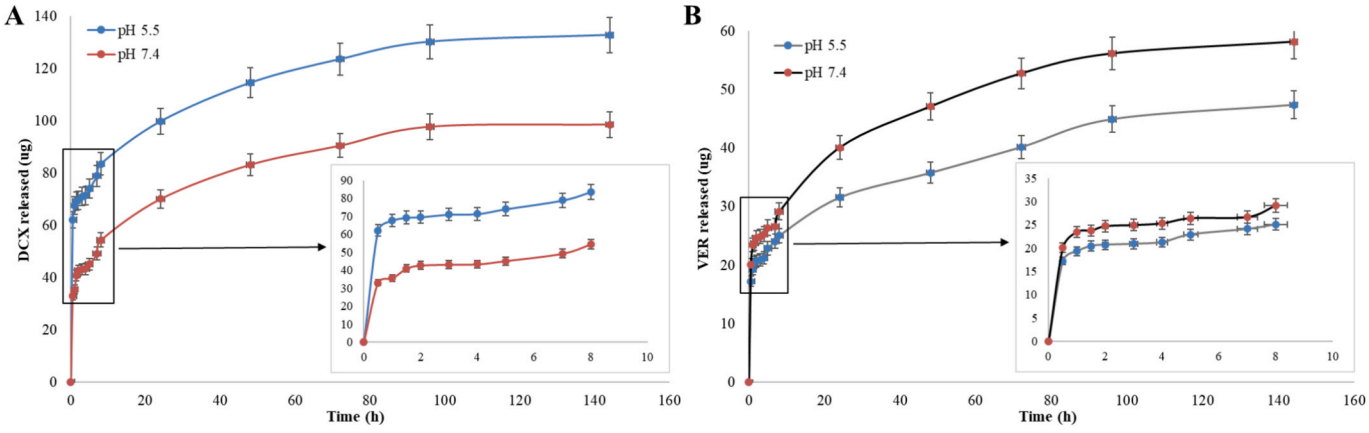

Fig. 4. The release pattern of DCX (A) and VER (B) from NP-DCX-VER.

2.8. Histological analysis

At each time point (0, 3, 7, 14 and 21 days) the rats were euthanized by anaesthesia hyper dose and afterwards the liver and kidney organs were collected, cut and fixed in 10% buffered formalin and embedded in parafine with a tissue processor Leica TP1020 (Leica Microsystems GmbH, Germany). Sections of 4 μm thickness were obtained with a SLEE CUT 6062 Microtome (SLEE Medical GmbH, Germany) and stained by the Masson trichrome techniques. The qualitative histology was performed from stained sections using Leica DM 1000 light microscope with

Table 2
Drug release kinetic parameters.

Released drug	pH	Zero-order			First-order			Higuchi			Korsmeyer-Peppas			
		k_0	RSS	R^2	k_1	RSS	R^2	k_H	RSS	R^2	n	k	RSS	R^2
DCX	5.5	0.8201	233.45	0.94	−0.0004	0.00005	0.94	7.906	37.1464	0.9904	0.1497	1.7928	0.0048	0.944
VER		0.2925	28.5559	0.9421	−0.0001	0.000054	0.9433	2.8203	3.3255	0.9933	0.1747	1.2545	0.0045	0.9607
DCX	7.4	0.7616	264.18	0.9227	−0.0004	0.000005	0.926	7.3935	48.3785	0.9858	0.2176	1.5386	0.0058	0.9675
VER		0.4356	47.5338	0.9559	−0.0002	0.000009	0.9572	4.1564	13.9733	0.987	0.2011	1.314	0.0126	0.9217

k_0: zero-order release constant, RSS: residual sum of squares, R^2: correlation coefficient, k_1: first-order release constant, k_H: Higuchi release constant, n: diffusional release exponent, k: Korsmeyer-Peppas release constant.

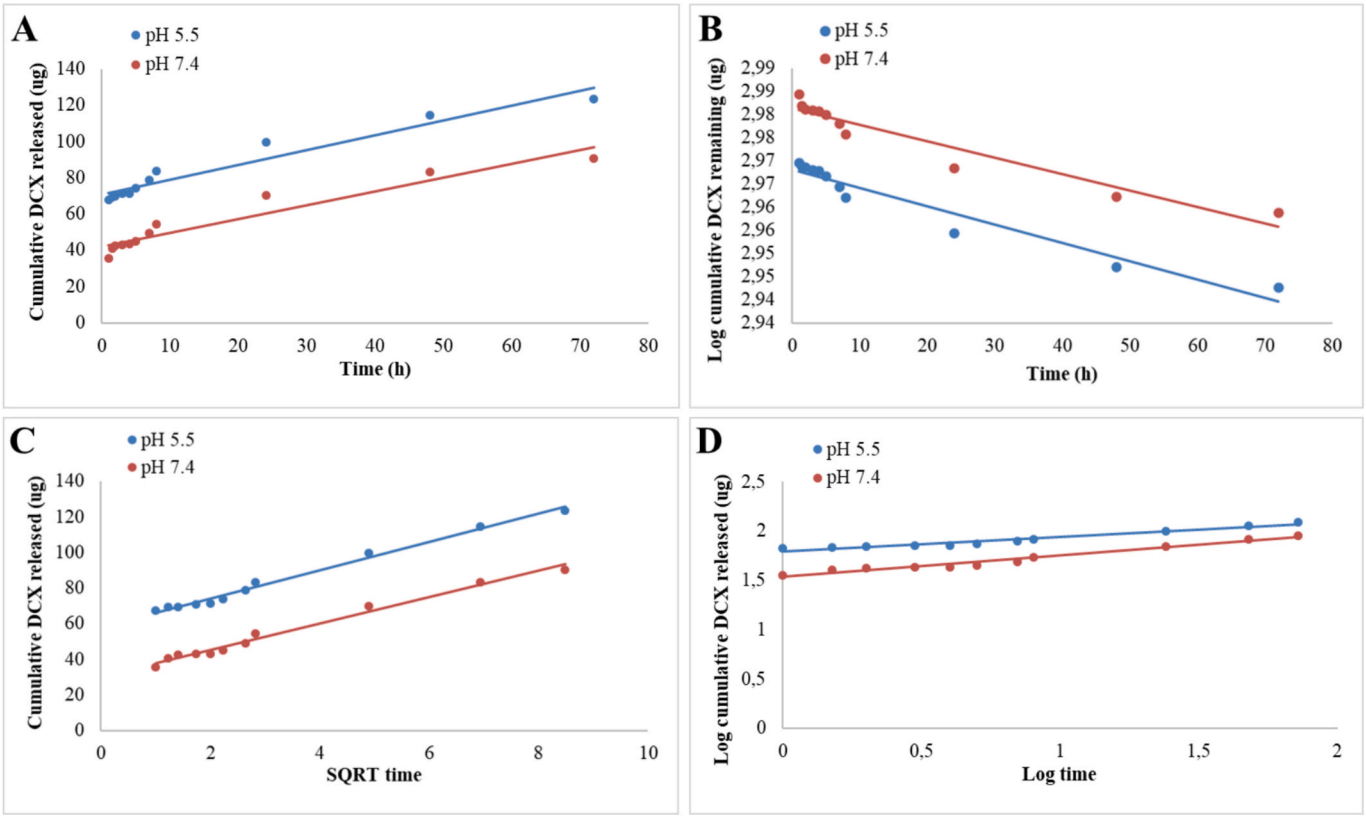

Fig. 5. Release kinetics graphs (A) zero-order, (B) first-order, (C) Higuchi, and (D) Korsemeyer-Peppas models of DCX from NP-DCX-VER.

an attached digital Leica ICC50 HD camera (Leica Microsystems GmbH, Germany). The photographs were acquired with Leica Application Suit Software (LAS), version 4.2.

2.9. Statistical analysis

All data were obtained in three independent triplicate experiments. Plotting and calculation of the standard deviation value were made using Microsoft Office Excel software, version 16.105. ANOVA test (single factor) was performed between nanoparticle groups *versus* saline controls, and p values less than 0.05 were considered statistically significant.

3. Results and discussions

3.1. Synthesis and characterization of fluorescent biotinylated N-palmitoyl chitosan (BPCs-FITC)

Fluorescent biotinylated N-palmitoyl chitosan (BPCs-FITC) was obtained through the reaction between biotinylated N-palmitoyl chitosan (BPCs) and fluorescein isothiocyanate (FITC), exploiting the facile conjugation of isothiocyanate (R–N=C=S) with amino groups ($–NH_2$) of the polymer, as depicted in Fig. 1A. Besides facile bonding, the use of FITC exhibits additional advantages, like water solubility, photo stability, good biocompatibility along with intense and stable fluorescence emission that allows easy detection of small nanoparticles (Huang et al., 2002; Zhao and Wu, 2006).

The successful synthesis of BPCs-FITC was confirmed through infrared spectroscopy (Fig. 2). The most representative bands from the IR spectrum of FITC (Fig. 2) were registered at: 3432 cm^{-1} (aromatic –OH groups), 2035 cm^{-1} (–N=C=S), 1596 cm^{-1}, 1535 cm^{-1}, 1462 cm^{-1} (stretching vibrations of benzene ring), 1113 cm^{-1} (ether bonds) (Khosroshahi and Asemani, 2017; Jiang et al., 2013). Likewise, FTIR spectrum of BPCs-FITC (Fig. 2) showed characteristic bands for biotinylated polymer at: 3419 cm^{-1} (O–H, N–H stretch, imidazole ring of biotin), 2919 cm^{-1} and 2872 cm^{-1} (stretching vibrations of methylene from palmitoyl chain), 1681 cm^{-1} (C=O), 1555 cm^{-1} (N–H) and 1376 cm^{-1} (C-N) (Serban et al., 2023; Ursachi et al., 2021), as well as for fluorescent marker (Khosroshahi and Asemani, 2017; Jiang et al., 2013). Also the absence of –N=C=S band, reinforce the successful conjugation of FITC, as a result of isothiocyanate conversion into thiourea group.

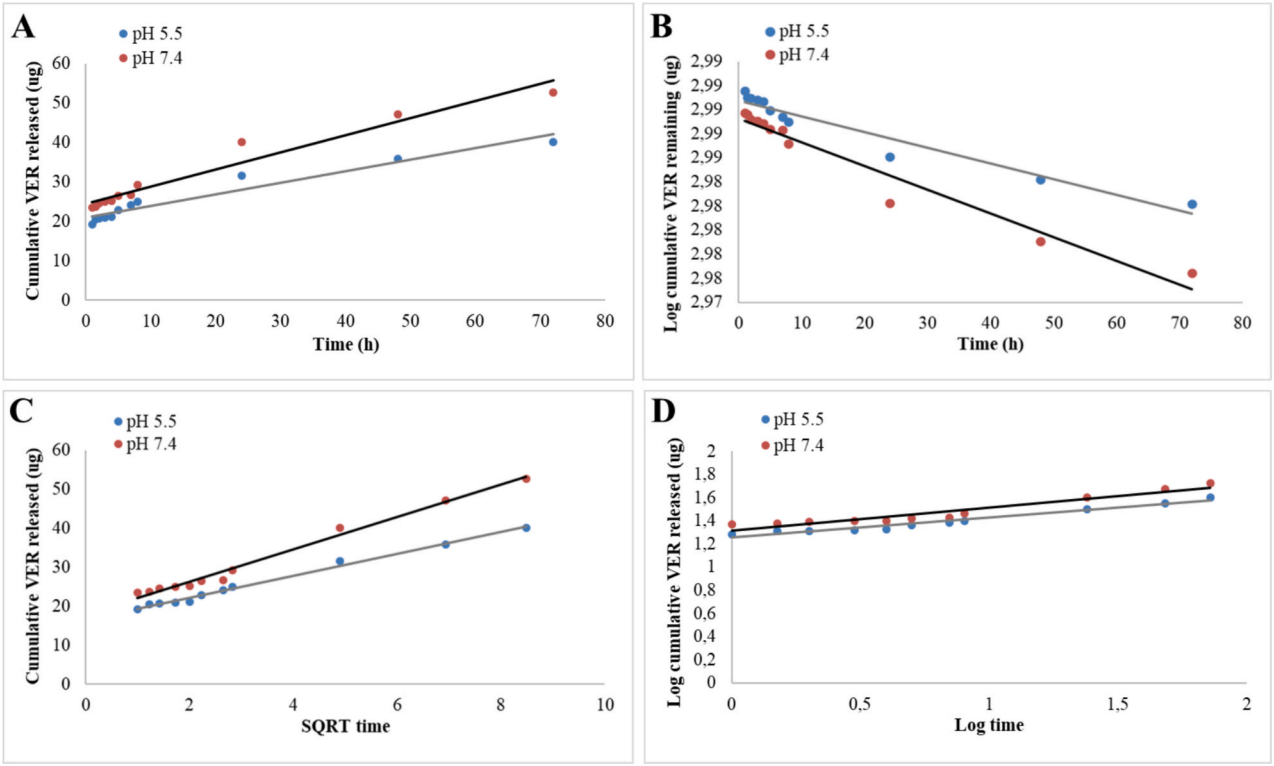

Fig. 6. Release kinetics graphs (A) zero-order, (B) first-order, (C) Higuchi, and (D) Korsemeyer-Peppas models of VER from NP-DCX-VER.

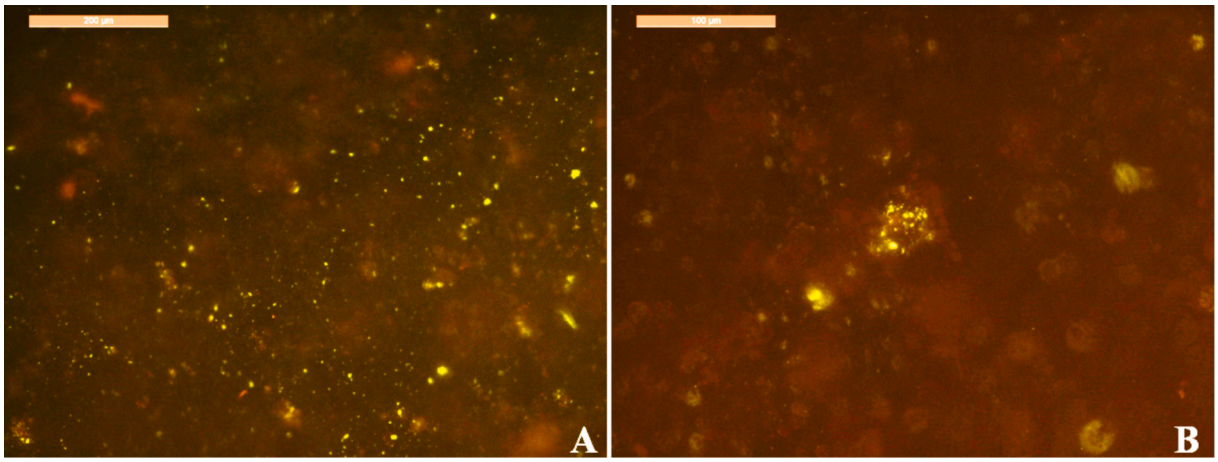

Fig. 7. Magnetic nanoparticles distribution within MCF-7 spheroids after 24 h.

3.2. Magnetic nanoparticles composition, morphology, size, surface charge and magnetic properties

With the aim to obtain co-encapsulated magnetic nanoparticles with a minimum average size and suitable drug loading, we combined self-assembly with ionic gelation (Fig. 1B). The self-assembly, promoted by ultrasonication, favoured the arrangement of amphiphile chitosan into micelles like nanostructures, formed by a hydrophobic core – advantageous for DCX encapsulation, and a hydrophilic outer layer, that can entrap aqueous soluble agents (Quiñones et al., 2018) as Verapamil. Furthermore, the additional electrostatic interactions established between the PO_4^{-3} and NH_3^+ groups, consequence of ionic gelation, fastened the co-encapsulated magnetic platform (Hoang et al., 2022).

The co-encapsulated magnetic nanoparticles composition was certified by infrared spectroscopy. Fig. 3A displays the IR spectrum of NP-DCX-VER, compared with the drugs spectra. The main IR bands of the DCX were recorded at: 3483 cm^{-1} (O–H stretching vibrations); 3337 cm^{-1} (N–H stretching vibrations); 2984 cm^{-1} (methylene stretching vibration); 1710 cm^{-1} (C=O stretching vibration of ester group); 1633 cm^{-1}, 1522 cm^{-1}, 1368 cm^{-1} (amide I, II, and respectively III bands); 1258 cm^{-1} (C–O band); 1070 cm^{-1} (C–O–C vibration); 981 and 708 cm^{-1} (aromatic bonds) (Balan et al., 2016; Sadaquat and Akhtar, 2020; Hammadi et al., 2017). In the IR spectrum of VER, were identified bands at 2957 and 2840 cm^{-1} (attributed to the stretching vibration of the methylene and methoxy groups), 2237 cm^{-1} (stretching of the C≡N group), 1599 and 1462 cm^{-1} (stretching of the benzene ring), 1258 cm^{-1} (C–O stretching vibration of aromatic ethers), 1149 cm^{-1} (vibration of the C-O-C ester group) (Abo Mansour et al., 2020). Similarly, NP-DCX-VER spectrum showed specific bands for the fluorescent biotinylated polymer, Docetaxel (1708 cm^{-1}, C=O of the ester group),

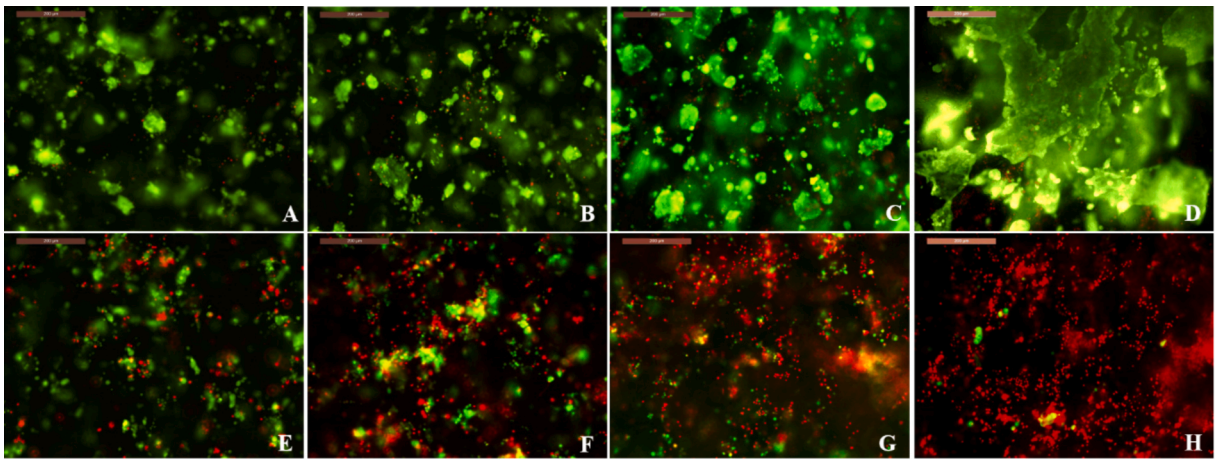

Fig. 8. Live/Dead assay for control spheroids at 24 h, 48 h, 72 h, 8 days (A-D) compared with spheroids treated with co-encapsulated magnetic nanoparticles (E-H); scale bar 20 μm.

Verapamil (2851 cm^{-1}, stretching vibration of the methoxy group) and magnetite (569 cm^{-1}, Fe–O group) and confirmed the co-encapsulation of drugs into the functionalized magnetic nanoplatform based on fluorescent BPCs.

The morphology of dried NP-DCX-VER, examined by transmission electron microscopy (Fig. 3C) revealed irregularly shaped, spherical nanoparticles with smooth surface and a tendency to assemble into grape-chain-like structures. Furthermore, TEM micrographs confirmed the effective encapsulation of magnetite nanoparticles (appearing as dark regions) within the biofunctionalized polymer matrix. Analysed in liquid form, in water, by DLS, the magnetic nanostructures suggested an average hydrodynamic mean diameter of 322.20 ± 2.50 nm, a polydispersity index (PDI) of 0.13 and a Zeta Potential value of 5.63 ± 0.16 mV for NP-DCX-VER, whilst the same parameters for NP were 294.8 ± 12.92 nm, 0.22 for PDI and respectively 2.14 ± 0.36 mV for Zeta Potential. In addition, the Zeta Potential of NP-DCX-VER redispersed in plasma simulated fluid, was 12.94 ± 0.20 mV.

It is important to clarify that TEM analysis revealed a primary magnetic core size of approximately 20 nm, indicating that the larger size observed by DLS arises from the formation of multicore nanoclusters rather than individual oversized nanoparticles. Minor sedimentation was observed during the experimental measurements; however, this aggregation proved to be reversible upon ultrasonication (3 min.). Furthermore, the hydrodynamic size includes contributions from the surface coating and solvation layer, which are known to increase the apparent particle diameter in liquid state.

A particle diameter of approximately 300 nm may be considered outside the optimal range for most systemic biomedical applications. Nanoparticles exceeding ~200 nm are readily identified by the mononuclear phagocyte system—specifically macrophages, hepatic Kupffer cells, and splenic filtration—leading to rapid systemic clearance and suboptimal intratumoral penetration (Tsoi et al., 2016 Nov; Laurent et al., 2010 Mar). While tumour vascular fenestrations are highly heterogeneous (ranging from 100 to 400 nm), 300 nm magnetic nanoparticles often remain sequestered in the perivascular space rather than achieving deep interstitial diffusion. Despite these limitations, the present particles demonstrated effective internalization within MCF-7 spheroids, likely facilitated by receptor-mediated endocytosis (Section 3.4). Furthermore, dimensions within the 100–400 nm range are consistent with previously reported magnetic nanoclusters optimized for enhanced hyperthermic efficiency and magnetic field responsiveness (Nitica et al., 2022). Additionally, larger particle profiles remain suitable for localized administration via intratumoral injection.

Superparamagnetic behaviour and good saturation magnetization are critical parameters for magnetic nanoparticles intended for biomedical applications. As shown in Fig. 3B, the magnetization curve of NP-DCX-VER demonstrates clear superparamagnetic characteristics, evidenced by the absence of hysteresis, with both remanent magnetization and coercivity equal to zero. In addition, the nanoparticles exhibited a good magnetic saturation of 13.35 emu/g.

3.3. *In vitro drug release*

Both active principles were successfully incorporated into magnetic nanoparticles, with a drug loading of 4% for DCX, and respectively 1.57% for VER. Drug release analyses, carried out in two simulated biological media (Fig. 4) disclosed a biphasic behaviour for both drugs, with an accelerated release pattern in the first 8 h, pursued by an upward trajectory. The initial burst release was associated with the drug molecules adsorbed at the nanoparticles surface (Jain et al., 2016; Tarasi et al., 2016), whereas the second phase ascribed a sustained delivery of the drugs entrapped into the core, because of polymer hydration and swelling (Mahmood et al., 2019). According to the Fig. 4A, a higher amount of DCX was released at pH 5.5 and indicated the nanoparticles' ability to be preferentially targeted to tumour cells. The release of VER (Fig. 4B), was faster than that of DCX, indicated that calcium channel blocker could be able to inhibit the efflux effect of P-gp, and lead to high anti-tumour activity and reversal drug resistance (Ashrafizadeh et al., 2023). Our results agree with other reports, concerning the pH-sensitive pattern of DCX–loaded nanoparticles (Zhang et al., 2019) and a faster release of VER, from co-encapsulated nanosystems (Baek and Cho, 2015).

Four well-known mathematical models, namely zero-order, first-order, Higuchi, and Korsmeyer-Peppas models, were used to describe the drug release mechanism from NP-DCX-VER. The drug release kinetic parameters are summarized in Table 2 and all plots are detailed in Figs. 5 and 6.

The Higuchi model provided the best fit across all formulations (R^2 = 0.9858–0.9933), indicating that drug release is predominantly governed by diffusion from a stable matrix-type system. This model assumes homogeneous drug distribution, negligible matrix erosion, and sink conditions, all of which are satisfied in the present system (Siepmann and Peppas, 2011). The Korsmeyer-Peppas model was applied exclusively to the initial 72 h, corresponding to Q_t/Q_∞ 0.6, in accordance with its theoretical limitations. The obtained diffusion exponent values (n = 0.1497–0.2176) are below the theoretical threshold for spherical systems (n≈ 0.43), confirming that drug release is controlled predominantly by Fickian diffusion (Ritger and Peppas, 1987; Siepmann and Peppas, 2012). Zero-order and first-order models were included for comparison. Their lower correlation coefficients and higher residual

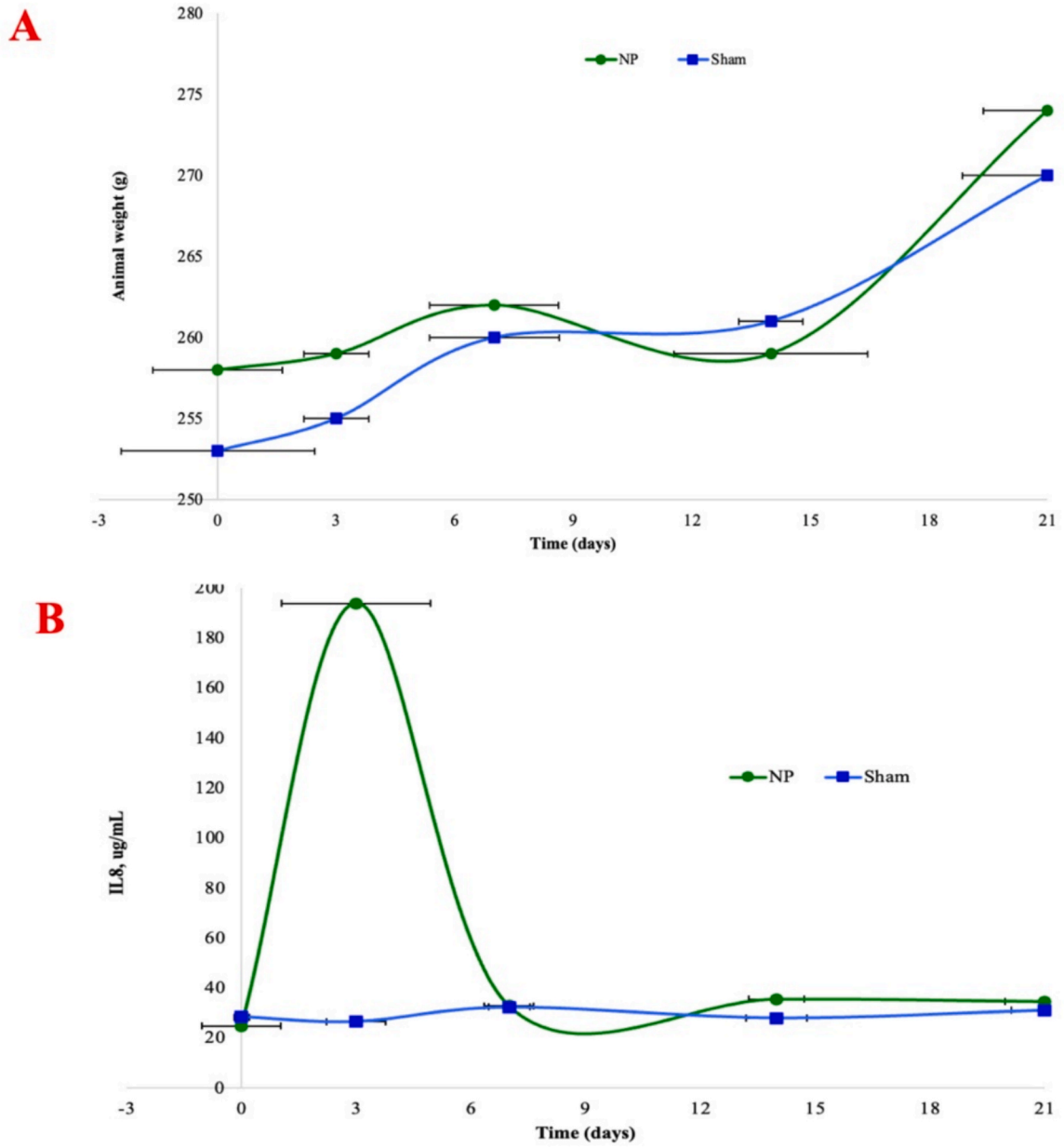

Fig. 9. Animals weight (A) and IL-8 concentration during the course of experiment for control (Sham) and treated group (3), 7, 14 and 21 days post-administration). Data presented as mean ± standard deviation. There was no significant difference among groups ($p > 0.05$).

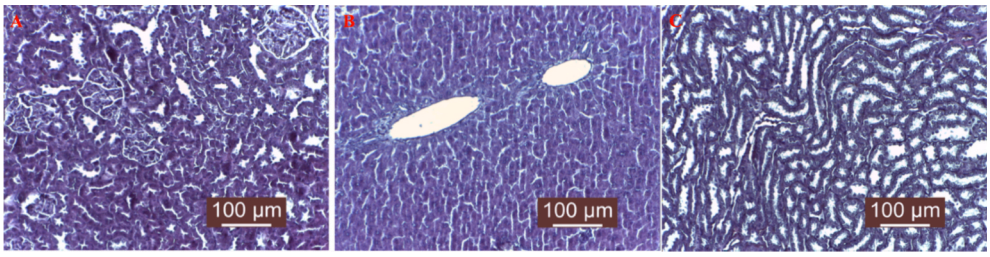

Fig. 10. Histological analysis (Masson trichrome staining) of liver (A), renal cortex (B) and renal medulla (C)- kidney tissues from the control group (Sham at day 0).

sum of squares support the conclusion that concentration-independent or simple first-order kinetics do not adequately describe this system. Therefore, it can be concluded that during the first 72 h, the release of the drug from NP-DCX-VER is primarily governed by diffusion rather than by other processes such as erosion or polymer relaxation.

3.4. In vitro cytotoxicity. Live/dead assay on MCF-7 spheroids

Three-dimensional (3D) culture systems, particularly spheroids, offer distinct advantages over conventional two-dimensional (2D) monolayer cultures for assessing anti-tumour drug efficacy. Spheroids

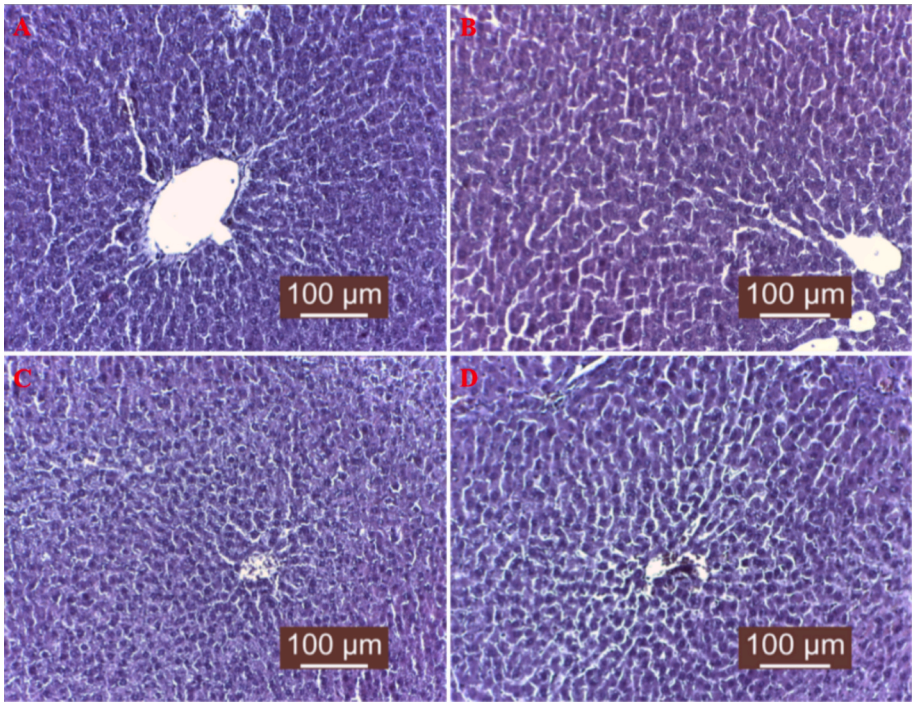

Fig. 11. Histological analysis (Masson trichrome staining) of liver tissues from NP-treated rats at: 3 (A), 7 (B), 14 (C) and 21 days (D) after *iv* administration.

accurately replicate key features of the *in vivo* tumour microenvironment, including gradients of nutrients, oxygen, and biochemical signalling molecules. As a result, they generate data with greater physiological relevance, reflecting the elevated drug resistance, typically exhibited by cells grown in 3D architectures relative to those maintained in 2D culture (Luca et al., 2021). In our previous work, we demonstrated that spheroids formed within collagen-based hydrogels provide a microenvironment that closely resembled the extracellular matrix (Luca et al., 2021). Based on this rationale, MCF-7 spheroids were produced by encapsulating cells in oxidized hyaluronic acid–crosslinked collagen hydrogels. Following confirmation of spheroid formation on day 6, co-encapsulated magnetic nanoparticles were added. Fig. 7 illustrates the distribution of these nanoparticles within the MCF-7 spheroids, visualized through the fluorescence emitted by conjugated FITC.

Cytotoxicity was evaluated at 24, 48, and 72 h, as well as on day 8, and compared with control spheroids encapsulated under identical conditions, but without nanoparticle treatment. As shown in Fig. 8 (A–D), control spheroids exhibited continuous cellular proliferation, resulting in well-defined spheroid architecture by day 6. In contrast, Fig. 8 (E–H) demonstrates a time-dependent increase in the dead-to-live cell ratio in spheroids treated with NP-DCX-VER, indicating a pronounced cytotoxic activity.

Cell viability in the treated groups was quantified through live/dead cell ratio, based on green- and red-fluorescent cell populations analysed in ImageJ (version 1.53 k). Viability analysis revealed a progressive decline throughout the treatment period: 48.97 ± 1.26% on day 1, decreasing to 30.14 ± 0.84% on day 2, 24.00 ± 0.15% on day 3, and 12.99 ± 0.06% by day 8. By the 8 day, more than 87% of cells within the spheroids were non-viable, confirming substantial treatment-induced cytotoxicity. These findings are consistent with prior MTT assay results, performed at 72 h, that indicated a clear advantage of the co-encapsulation strategy. Specifically, cell viability decreased to 25.24 ± 0.78% following exposure to NP-DCX-VER, compared with 68.63 ± 1.92% for NP-DCX and 79.86 ± 2.40% for NP-VER.

3.5. In vivo toxicity of drug-free magnetic nanoparticles. Enzyme-linked immunosorbent assay (ELISA)

To examine *in vivo* effects of drug-free magnetic nanoparticles, these were administered by single intravenous injection to allow maximum bioavailability. The survival rate over 21 days post injection was 100%. No signs of distress, such as loss of hair or behavioural changes were observed by Grimace scale. Animal body weight was monitored during the experiments and the graph presented in Fig. 9A illustrates the fact that magnetic nanoparticles did not alter the general health of the animals. The weight gain rate of the NPs treated animals followed the same pattern as the control group. No significant differences were observed among the control and nanoparticles treated groups in the weight gain, as obtained by ANOVA single factor analysis, where p value was found to be 0.552, greater than 0.05, considered the threshold.

An initial step in the *in vivo* evaluation of the magnetic nanoparticles behaviour was represented by the quantification of IL-8 levels produced exclusively as response to the presence of the magnetic nanostructures, in the absence of any drug, employing ELISA technique. The IL-8 levels, shown in Fig. 9B, evaluated the inflammation and immune modulation of the rats upon the magnetic nanoparticles *iv* administration, two major events in nanoparticles-mediated toxicities detected by blood cytokines measurement (Luo et al., 2015).

For the untreated control group, the serum IL-8 level showed relatively no differences in all time-points. For the NP-treated group, IL-8 level was increased from 24.83 ± 1.04 pg/mL in day 0 to 193.90 ± 1.94 pg/mL at day 3, indicating that intravenous administration of magnetic nanoparticles induces an acute inflammatory response. This increased level of serum inflammatory cytokine may be responsible for the inflammation-induced oxidative stress, as described in the literature, since nanomaterials can reach mitochondria and hence may induce inflammatory response in activated macrophages with the production of reactive oxygen species (He et al., 2018). In the subacute phase (at 7 and 14 days), the cytokine levels decreased to 32.78 ± 0.64 and 35.53 ± 0.73 pg/mL, respectively, suggesting that the release of pro-inflammatory cytokines was diminished. A similar activity was observed also for the post-acute phase, at 21 days after the NP-treatment, with a value of 34.55 ± 1.02 pg/mL, comparable with the

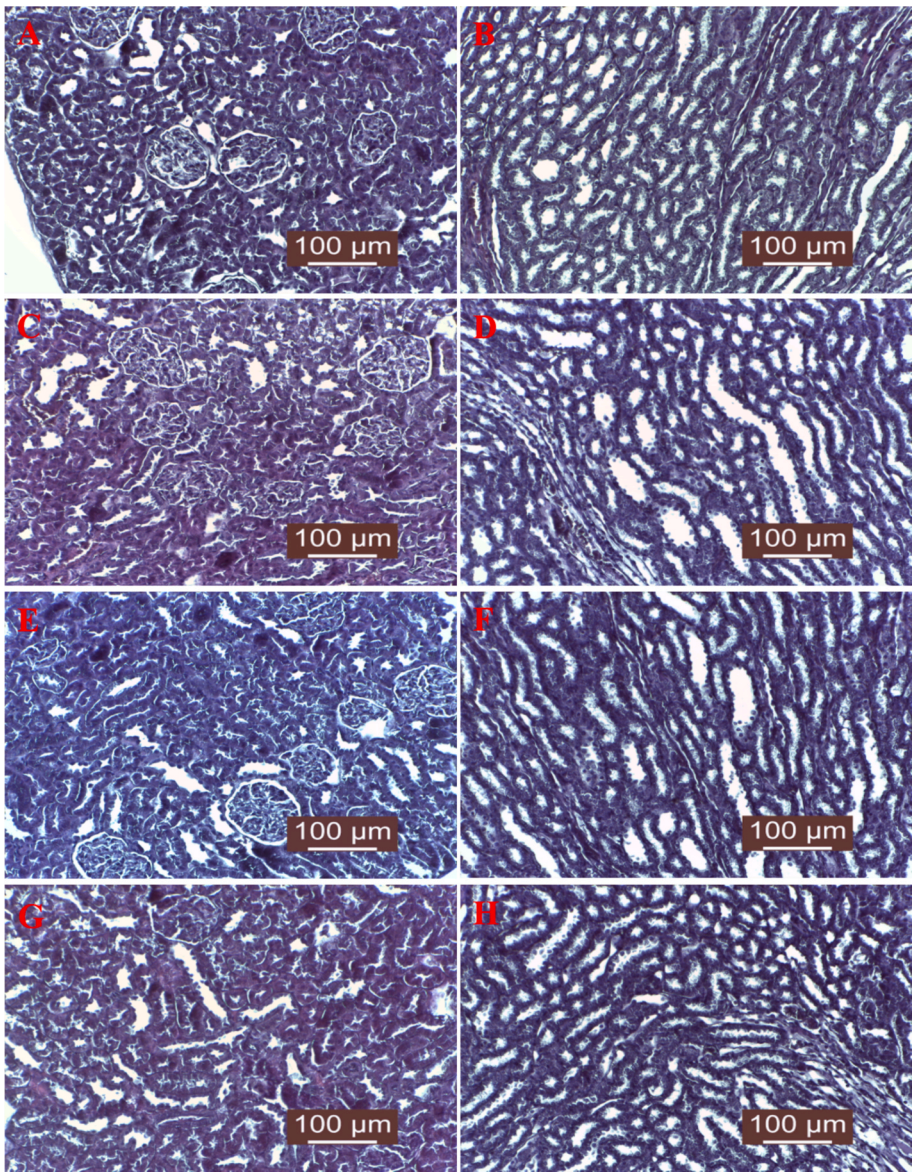

Fig. 12. Histologic analysis (Masson trichrome staining) of kidney tissues from NP-treated rats at: 3 days (A. renal cortex and B. renal medulla); 7 days (C. renal cortex and D. renal medulla); 14 days (E. renal cortex and F. renal medulla) and 21 days (G. renal cortex and H. renal medulla) after *iv* administration.

control group at the same period of time (31.12 ± 0.87 pg/mL). The values represent the mean ± standard deviation with p value of 0.3, calculated from the source of variation between groups (one-way ANOVA), meaning than p is not <0.05, expressed a clear lack of significant change in the serum IL-8 values, following nanoparticles injection. These findings have substantial implications in the biocompatibility of the drug-free magnetic nanoparticles.

3.6. Histopathological changes due to magnetic nanoparticles

Next, we evaluated the effects of the NPs on the hepatic and renal tissues of rats. Photomicrographs of the control group demonstrated normal histological architecture of the liver (Masson trichrome staining), characterized by hepatocytes arranged in regular cords and separated by intact blood sinusoids (Fig. 10A). Likewise, the photomicrographs presented in Fig. 10B,C for the control rats showed normal renal histology, including well-defined glomeruli and tubular structures.

Microscopic examination of liver sections from treated animals revealed no observable morphological alterations relative to the control group. Hepatocytes appeared structurally intact, indicating preserved cellular integrity across all exposure periods, including the acute (Fig. 11A), subacute (Fig. 11,C), and post-acute phases (Fig. 11D). Kidney histopathology (Fig. 12), showed that the exposure of NPs did not cause pathological changes in the renal cortex and medulla with no infiltration of inflammatory cells, as denoted by the blood serum cytokine levels in the acute exposure. However, these NPs were consumed by macrophages and probably were not eliminated from the body via nephrocytes, to produce alterations. The results suggest that the nanoparticles did not exacerbate the pathological changes in the liver or kidney, indicating the protective capacity building in these animals against the exposure of the NPs, in agreement with previous reports that showed the absence of toxicity in animals treated with DMSA-coated magnetic nanoparticles (Paulini et al., 2022).

4. Conclusions

This study contributes to the development of drug-loaded magnetic nanoparticles with potential applications in breast cancer therapy by exploiting co-encapsulation strategies. Co-encapsulated magnetic

nanoparticles based on fluorescent biotinylated N-palmitoyl chitosan were successfully synthesized for the first time, via a two-step process involving ultrasonication-induced self-assembly followed by ionic gelation. Their composition was confirmed by infrared spectroscopy. The magnetic nanostructures exhibited an average hydrodynamic diameter of 322.20 ± 2.50 nm, positive surface charge and good magnetic properties. Drug release studies conducted in two simulated biological media demonstrated a pH-sensitive release profile for both active pharmaceutical agents (Docetaxel and Verapamil), with a faster release of the calcium channel blocker, which may inhibit P-glycoprotein efflux, enhance anti-tumour efficacy, and potentially reverse drug resistance. Live/dead assays performed on MCF-7 spheroids cultured within collagen-based hydrogels indicated a significant cytotoxic effect over an 8-day period. Preliminary *in vivo* studies, expressed by serum IL-8 levels, as response to the presence of the magnetic nanostructures, in the absence of any drug, demonstrated good biocompatibility. Collectively, these results indicate that the newly designed magnetic nanoplatforms hold promising potential for breast cancer therapy. Further comprehensive investigations are required to confirm the P-glycoprotein inhibition capacity of the proposed system. In addition, *in vivo* evaluation of the co-encapsulated formulations is necessary to elucidate the action mechanism of therapeutic agents and their pharmacologic activity.

CRediT authorship contribution statement

Stefan Sandu: Writing – review & editing, Writing – original draft, Investigation, Formal analysis, Data curation. **Gianina Dodi:** Writing – review & editing, Writing – original draft, Investigation, Formal analysis, Data curation. **Ioannis Gardikiotis:** Writing – original draft, Investigation, Formal analysis, Data curation. **Bianca-Elena Cretu:** Writing – review & editing, Writing – original draft, Investigation, Formal analysis, Data curation. **Andreea Luca:** Writing – review & editing, Writing – original draft, Investigation, Formal analysis, Data curation. **Florina Daniela Cojocaru:** Writing – review & editing, Writing – original draft, Investigation, Formal analysis, Data curation. **Liliana Verestiuc:** Resources, Formal analysis, Data curation. **Sorin-Aurelian Pasca:** Investigation, Formal analysis, Data curation. **Vera Balan:** Writing – review & editing, Writing – original draft, Validation, Supervision, Resources, Project administration, Methodology, Investigation, Funding acquisition, Formal analysis, Data curation, Conceptualization.

Declaration of competing interest

The authors declare that they have no known competing financial interests or personal relationships that could have appeared to influence the work reported in this paper.

Acknowledgments

This work was supported by a grant of the Ministry of Research, Innovation and Digitization, CNCS/CCCDI – UEFISCDI, project number PN-III-P1-1.1-TE-2019-1671, within PNCDI III.

Data availability

The data analysed during the current study are available from the corresponding author upon reasonable request.

References

Abo Mansour, H.E., El-Batsh, M.M., Badawy, N.S., Mehanna, E.T., Mesbah, N.M., Abo-Elmatty, D.M., 2020. Effect of co-treatment with doxorubicin and verapamil loaded into chitosan nanoparticles on diethylnitrosamine-induced hepatocellular carcinoma in mice. Hum. Exp. Toxicol. 39 (11), 1528–1544. https://doi.org/10.1177/0960327120930266.

Aravindan, A., Gupta, A., Moorkoth, S., Dhas, N., 2024. Implications of nanotherapeutic advancements to leverage multi-drug resistant breast cancer: the state-of-the-art review. J. Drug Deliv. Sci. Technol. 100, 106007. https://doi.org/10.1016/j.jddst.2024.106007.

Arısoy, S., Comoglu, T., 2020. Kinetic evaluation of L-Dopa loaded WGA-grafted nanoparticles. Med-Science 9 (2), 385–388. https://doi.org/10.5455/medscience.2019.08.9209.

Ashrafizadeh, M., Zarrabi, A., Bigham, A., et al., 2023. (Nano)platforms in breast cancer therapy: drug/gene delivery, advanced nanocarriers and immunotherapy. Med. Res. Rev. 43, 2115–2176. https://doi.org/10.1002/med.21971.

Avendano, C., Menéndez, J.C., 2002. Inhibitors of multidrug resistance to antitumor agents (MDR). Curr. Med. Chem. 9 (2), 159–193. https://doi.org/10.2174/0929867023371175.

Baek, J.S., Cho, C.W., 2015. Controlled release and reversal of multidrug resistance by co-encapsulation of paclitaxel and verapamil in solid lipid nanoparticles. Int. J. Pharm. 478 (2), 617–624. https://doi.org/10.1016/j.ijpharm.2014.12.018.

Balan, V., Redinciuc, V., Tudorachi, N., Verestiuc, L., 2016. Biotinylated N-Palmitoyl Chitosan for Design of Drug Loaded Self-Assembled Nanocarriers. Eur. Polym. J. 81, 284–294. https://doi.org/10.1016/j.eurpolymj.2016.06.014.

Balan, V., Dodi, G., Mihai, C.T., Serban, A.M., Ursachi, V.C., 2021. Biotinylated chitosan macromolecule based nanosystems: a review from chemical design to biological targets. Int. J. Biol. Macromol. 188, 82–93. https://doi.org/10.1016/j.ijbiomac.2021.07.197.

Barzaman, K., Karami, J., Zarei, Z., Hosseinzadeh, A., Kazemi, M.H., Moradi-Kalbolandi, S., Safari, E., Farahmand, L., 2020. Breast cancer: biology, biomarkers, and treatments. Int. Immunopharmacol. 84, 106535. https://doi.org/10.1016/j.intimp.2020.106535.

Cheng, X., et al., 2019. Co-delivery of DOX and PDTC by pH-sensitive nanoparticles to overcome multidrug resistance in breast cancer. Colloids Surf. B Biointerfaces 181, 185–197. https://doi.org/10.1016/j.colsurfb.2019.05.042.

Cui, F., Liu, J., Pang, S., Li, B., 2022. Recent advance in tumor microenvironment-based stimuli-responsive nanoscale drug delivery and imaging platforms. *Front. Pharmacol.* 13, 929854. https://doi.org/10.3389/fphar.2022.929854.

Da Silva, G.H., Fernandes, M.A., Trevizan, L.N.F., De Lima, F.T., Eloy, J.O., Chorilli, M., 2018. A critical review of properties and analytical methods for the determination of docetaxel in biological and pharmaceutical matrices. Crit. Rev. Anal. Chem. 48 (6), 517–527. https://doi.org/10.1080/10408347.2018.1456315.

Das, T., Anand, U., Pandey, S.K., Ashby Jr, C.R., Assaraf, Y.G., Chen, Z.S., Dey, A., 2021. Therapeutic strategies to overcome taxane resistance in cancer. Drug Resist. Updat. 55, 100754. https://doi.org/10.1016/j.drup.2021.100754.

Demiral, A., Goralı, S.I., Yılmaz, H., et al., 2022. Stimuli-responsive theranostic system: a promising approach for augmented multimodal imaging and efficient drug release. Eur. J. Pharm. Biopharm. 177, 9–23. https://doi.org/10.1016/j.ejpb.2022.05.021.

Dodi, G., Hritcu, D., Draganescu, D., Popa, M.I., 2015. Iron oxide nanoparticles for magnetically assisted patterned coatings. J. Magn. Magn. Mater. 388, 49–58. https://doi.org/10.1016/j.jmmm.2015.04.011.

Gote, V., Nookala, A.R., Bolla, P.K., Pal, D., 2021. Drug resistance in metastatic breast cancer: tumor targeted nanomedicine to the rescue. Int. J. Mol. Sci. 22 (9), 4673. https://doi.org/10.3390/ijms22094673.

Graham, W., Torbett-Dougherty, M., Islam, A., Soleimani, S., Bruce-Tagoe, T.A., Johnson, J.A., 2025. Magnetic nanoparticles and drug delivery systems for anti-cancer applications: a review. Nanomaterials 15, 285. https://doi.org/10.3390/nano15040285.

Guo, Y., He, W., Yang, S., Zhao, D., Li, Z., Luan, Y., 2017. Co-delivery of docetaxel and verapamil by reduction-sensitive PEG-PLGA-SS-DTX conjugate micelles to reverse the multi-drug resistance of breast cancer. Colloids Surf. B Biointerfaces 151, 119–127. https://doi.org/10.1016/j.colsurfb.2016.12.012.

Guo, Y., Qiao, D., Zhao, S., Liu, P., Xie, F., Zhang, B., 2024. Biofunctional chitosan–biopolymer composites for biomedical applications. Mater. Sci. Eng. R. Rep. 159, 100775. https://doi.org/10.1016/j.mser.2024.100775.

Hammadi, N.I., Abba, Y., Hezmee, M.N.M., et al., 2017. Formulation of a sustained release docetaxel loaded cockle shell-derived calcium carbonate composites against breast cancer. Pharm. Res. 34 (6), 1193–1203. https://doi.org/10.1007/s11095-017-2135-1.

He, C., Jiang, S., Yao, H., Zhang, L., Yang, C., Zhan, D., Lin, G., Zeng, Y., Xia, Y., Lin, Z., Liu, G., 2018. Endoplasmic reticulum stress mediates inflammatory response triggered by ultra-small superparamagnetic iron oxide nanoparticles in hepatocytes. Nanotoxicology 12 (10), 1198–1214. https://doi.org/10.1080/17435390.2018.1530388.

Heredia, N.S., Vizuete, K., Flores-Calero, M., Pazmiño, V.K., Pilaquinga, F., Kumar, B., Debut, A., 2022. Comparative statistical analysis of the release kinetics models for nanoprecipitated drug delivery systems based on poly(lactic-co-glycolic acid). PLoS One 17 (3). https://doi.org/10.1371/journal.pone.0264825.

Hoang, N.H., Le Thanh, T., Sangpueak, R., et al., 2022. Chitosan nanoparticles-based ionic gelation method: a promising candidate for plant disease management. Polymers 14 (4), 662. https://doi.org/10.3390/polym14040662.

Holohan, C., et al., 2013. Cancer drug resistance: an evolving paradigm. Nat. Rev. Cancer 13 (10), 714–726. https://doi.org/10.1038/nrc3599.

Huang, M., Ma, Z., Khor, E., Lim, L.Y., 2002. Uptake of FITC-chitosan nanoparticles by A549 cells. Pharm. Res. 19 (10), 1488–1494. https://doi.org/10.1023/a:1020404615898.

Imran, M., Saleem, S., Chaudhuri, A., Ali, J., Baboota, S., 2020. Docetaxel: an update on its molecular mechanisms, therapeutic trajectory and nanotechnology in the treatment of breast, lung and prostate cancer. J. Drug Deliv. Sci. and Technol. 60, 101959. https://doi.org/10.1016/j.jddst.2020.101959.

Jain, A., Thakur, K., Sharma, G., Kush, P., Jain, U.K., 2016. Fabrication, characterization and cytotoxicity studies of ionically cross-linked docetaxel loaded chitosan nanoparticles. Carbohydr. Polym. 137, 65–74. https://doi.org/10.1016/j.carbpol.2015.10.012.

Jaiswal, S., Dutta, P.K., Kumar, S., Chawla, R., 2021. Chitosan modified by organo-functionalities as an efficient nanoplatform for anti-cancer drug delivery process. J. Drug Deliv. Sci. Technol. 62, 102407. https://doi.org/10.1016/j.jddst.2021.102407.

Jiang, L., Li, X., Liu, L., Zhang, Q., 2013. Cellular uptake mechanism and intracellular fate of hydrophobically modified pullulan nanoparticles. Int. J. Nanomed. 8, 1825–1834. https://doi.org/10.2147/ijn.s44342.

Khosroshahi, M.E., Asemani, M., 2017. Synthesis, characterization and imaging of fluorescine isothiocyanate conjugated magnetite nanoparticles in MCF-7 breast cancer cell lines. Int. J. Nanomater. Nanotechnol. Nanomed. 3 (2), 044–050. https://doi.org/10.17352/2455-3492.000020.

Korsmeyer, R.W., Gurny, R., Doelker, E., Buri, P., Peppas, N.A., 1983. Mechanisms of solute release from porous hydrophilic polymers. Int. J. Pharm. 15 (1), 25–35. https://doi.org/10.1016/0378-5173(83)90064-9.

Laurent, S., Bridot, J.L., Elst, L.V., Muller, R.N., 2010 Mar. Magnetic iron oxide nanoparticles for biomedical applications. Future Med. Chem. 2 (3), 427–449. https://doi.org/10.4155/fmc.09.164.

Lepeltier, E., Rijo, P., Rizzolio, F., Popovtzer, R., Petrikaite, V., Assaraf, Y.G., Passirani, C., 2020. Nanomedicine to target multidrug resistant tumors. Drug Resist. Updat. 52, 100704. https://doi.org/10.1016/j.drup.2020.100704.

Liu, H.Q., Wu, X.D., Fang, X.W., An, Y.S., Xia, M., Luo, X.H., Li, J.Z., Wang, G.H., Liu, T., 2024. Tumor-targeted magnetic micelles for magnetic resonance imaging, drug delivery, and overcoming multidrug resistance. ACS Omega 9 (50), 49566–49579. https://doi.org/10.1021/acsomega.4c07132.

Lu, S., Xu, L., Kang, E.T., Mahendran, R., Chiong, E., Neoh, K.G., 2016. Co-delivery of peptide-modified cisplatin and doxorubicin via mucoadhesive nanocapsules for potential synergistic intravesical chemotherapy of non-muscle-invasive bladder cancer. Eur. J. Pharm. Sci. 84, 103–115. https://doi.org/10.1016/j.ejps.2016.01.013.

Luca, A., Craescu, T., Verestiuc, L., M. Butnaru, Mimicking In Vivo Tissue Microenvironment for In Vitro Testing – Hydrogels for Cell Encapsulation, Nanotechnologies and Biomedical Engineering, in Springer International Publishing, 5 (2021) 89, ISBN 978-9975-72-592-7.

Luo, Y.H., Chang, L.W., Lin, P., 2015. Metal-based nanoparticles and the immune system: activation, inflammation, and potential applications. Biomed Res. Int. 2015, 143720. https://doi.org/10.1155/2015/143720.

Mahmood, M.A., Madni, A., Rehman, M., Rahim, M.A., Jabar, A., 2019. Ionically cross-linked chitosan nanoparticles for sustained delivery of docetaxel: fabrication, post-formulation and acute oral toxicity evaluation. Int. J. Nanomed. 14, 10035–10046. https://doi.org/10.2147/ijn.s232350.

Mi, P., 2020. Stimuli-responsive nanocarriers for drug delivery, tumor imaging, therapy and theranostics. Theranostics 10, 4557–4588. https://doi.org/10.7150/thno.38069.

Nitica, S., Fizesan, I., Dudric, R., Loghin, F., Lucaciu, C.M., Iacovita, C., 2022. Doxorubicin loaded thermosensitive magneto-liposomes obtained by a gel hydration technique: characterization and in vitro magneto-chemotherapeutic effect assessment. Pharmaceutics 14, 2501. https://doi.org/10.3390/pharmaceutics14112501.

Nivethaa, E.A.K., Sivasankari, J., Baskar, S., Martin, C.A., Narayana Kalkura, S., 2025. Folic acid conjugated magnetic chitosan nanocomposite for the targeted delivery of dual anticancer drugs to breast cancer and hyperthermia therapy. Int. J. Biol. Macromol. 327, 147303. https://doi.org/10.1016/j.ijbiomac.2025.147303.

Paarakh, M.P., Jose, P.A., Setty, C.M., Christoper, G.V., 2018. Release kinetics—concepts and applications. Int. J. Pharm. Res. Technol. 8 (1). https://doi.org/10.31838/ijprt/08.01.02.

Panthi, V.K., Bashyal, S., Paudel, K.R., 2023. Docetaxel-loaded nanoformulations delivery for breast cancer management: challenges, recent advances, and future perspectives. J. Drug Deliv. Sci. Technol. 92, 105314. https://doi.org/10.1016/j.jddst.2023.105314.

Pareek, A., Alasiri, G., Dudhwala, Y., Alaseem, A.M., Alsaidan, O.A., Kapoor, D.U., Prajapati, B.G., 2025. Review of engineered magnetic chitosan nanoparticles for drug delivery: advances, challenges, and future prospects. Int. J. Biol. Macromol. 327, 147441. https://doi.org/10.1016/j.ijbiomac.2025.147441.

Pareek, A., Kumar, S., Kapoor, D.U., Prajapati, B.G., 2025. Advancements in superparamagnetic nanogels: a dual-role platform for diagnosis and targeted drug delivery. Int. J. Pharm. 677, 125683. https://doi.org/10.1016/j.ijpharm.2025.125683.

Park, J.H., Im, S.A., Byun, J.M., Kim, K.H., Kim, J.S., Choi, I.S., Kim, H.J., Lee, K.H., Kim, T.Y., Han, S.W., Oh, D.Y., Kim, T.Y., 2017. Cyclophosphamide, methotrexate, and 5-fluorouracil as palliative treatment for heavily pretreated patients with metastatic breast cancer: a multicenter retrospective analysis. J. Breast Cancer 20 (4), 347–355. https://doi.org/10.4048/jbc.2017.20.4.347.

Paulini, F., Marangon, A.R.M., Azevedo, C.L., Brito, J.L.M., Lemos, M.S., Sousa, M.H., Veiga-Souza, F.H., Souza, P.E.N., Lucci, C.M., Azevedo, R.B., 2022. In vivo evaluation of DMSA-coated magnetic nanoparticle toxicity and biodistribution in rats: a long-term follow-up. Nanomaterials 12 (19), 3513. https://doi.org/10.3390/nano12193513.

Payamifar, S., Khalili, Y., Foroozandeh, A., Abdouss, M., Hasanzadeh, M., 2025. Magnetic mesoporous silica nanoparticles as advanced polymeric scaffolds for efficient cancer chemotherapy: recent progress and challenges. RSC Adv. 15 (20), 16050–16074. https://doi.org/10.1039/d5ra00948k.

Quiñones, J.P., Peniche, H., Peniche, C., 2018. Chitosan based self-assembled nanoparticles in drug delivery. Polymers 10 (3), 235. https://doi.org/10.3390/polym10030235.

Rahmanian, M., Seyfoori, A., Ghasemi, M., Shamsi, M., Kolahchi, A.R., Modarres, H.P., Sanati-Nezhad, A., Majidzadeh-A, K., 2021. In-vitro tumor microenvironment models containing physical and biological barriers for modelling multidrug resistance mechanisms and multidrug delivery strategies. J. Control. Release 334, 164–177. https://doi.org/10.1016/j.jconrel.2021.04.024.

Ritger, P.L., Peppas, N.A., 1987. A simple equation for description of solute release II. Fickian and anomalous release from swellable devices. J. Control. Release 5 (1), 37–42. https://doi.org/10.1016/0168-3659(87)90035-6.

Sadaquat, H., Akhtar, M., 2020. Comparative effects of β-cyclodextrin, HP-β-cyclodextrin and SBE7-β-cyclodextrin on the solubility and dissolution of docetaxel via inclusion complexation. J. Incl. Phenom. Macrocycl. Chem. 96, 333–351. https://doi.org/10.1007/s10847-020-00977-0.

Sanchez-Orozco, J.L., Garcia-Cerda, L.A., Puente-Urbina, B., Ortiz, H.I.M., 2023. Poly (Nvinylcaprolactam-co-2-(diethylamino) ethylmethacrylate) coated Fe3O4@SiO2 core-shell magnetic nanoparticles for controlled doxorubicin delivery. J. Drug Deliv. Sci. Technol. 81, 104253. https://doi.org/10.1016/j. jddst.2023.104.

Serban, A.M., Ursachi, V.C., Verestiuc, L., Dodi, G., Balan, V., 2023. Synthesis and evaluation of novel Docetaxel-loaded magnetic composites based on chitosan biotinylated derivative. Mater. Lett. 333, 133592. https://doi.org/10.1016/j.matlet.2022.133592.

Siepmann, J., Peppas, N.A., 2011. Higuchi equation: Derivation, applications, use and misuse. Int. J. Pharm. 418 (1), 6–12. https://doi.org/10.1016/j.ijpharm.2011.03.051.

Siepmann, J., Peppas, N.A., 2012. Modeling of drug release from delivery systems based on hydroxypropyl methylcellulose (HPMC). Adv. Drug Deliv. Rev. 64, 163–174. https://doi.org/10.1016/j.addr.2012.09.028.

Su, Z., Dong, S., Zhao, S.C., Liu, K., Tan, Y., Jiang, X., Assaraf, Y.G., Qin, B., Chen, Z.S., Zou, C., 2021. Novel nanomedicines to overcome cancer multidrug resistance. Drug Resist. Updat. 58, 100777. https://doi.org/10.1016/j.drup.2021.100777.

Tan, L.K., How, C.W., Low, L.E., Ong, B.H., Loh, J.S., Lim, S.-Y., Ong, Y.S., Foo, J.B., 2023. Magnetic-guided targeted delivery of zerumbone/SPION co-loaded in nanostructured lipid carrier into breast cancer cells. J Drug Deliv Sci Technol. 87, 104830. https://doi.org/10.1016/j.jddst.2023.104830.

Tang, H., Chen, J., Wang, L., Li, Q., Yang, Y., Lv, Z., Bao, H., Li, Y., Luan, X., Li, Y., et al., 2020. Co-delivery of epirubicin and paclitaxel using an estrone-targeted PEGylated liposomal nanoparticle for breast cancer. Int. J. Pharm. 573, 118806. https://doi.org/10.1016/j.ijpharm.2019.118806.

Tarasi, R., Khoobi, M., Niknejad, H., Ramazani, A., Ma'mani, L., Bahadorikhalili, S., Shafiee, A., 2016. β-Cyclodextrin functionalized poly (5-amidoisophthalicacid) grafted Fe3O4 magnetic nanoparticles: a novel biocompatible nanocomposite for targeted docetaxel delivery. J. Magn. Magn. Mater. 417, 451–459. https://doi.org/10.1016/j.jmmm.2016.05.080.

Tian, F., Dahmani, F.Z., Qiao, J., Ni, J., Xiong, H., Liu, T., Zhou, J., Yao, J., 2018. A targeted nanoplatform co-delivering chemotherapeutic and antiangiogenic drugs as a tool to reverse multidrug resistance in breast cancer. Acta Biomater. 75, 398–412. https://doi.org/10.1016/j.actbio.2018.05.050.

Tsoi, K.M., MacParland, S.A., Ma, X.Z., Spetzler, V.N., Echeverri, J., Ouyang, B., Fadel, S. M., et al., 2016 Nov. Mechanism of hard-nanomaterial clearance by the liver. Nat. Mater. 15 (11), 1212–1221. https://doi.org/10.1038/nmat4718.

Ursachi, V.C., Dodi, G., Rusu, A.G., Mihai, C.T., Verestiuc, L., Balan, V., 2021. Paclitaxel-loaded magnetic composites based on biotinylated N-palmitoyl chitosan: synthesis, characterization and preliminary in vitro studies. Molecules 26 (11), 3467. https://doi.org/10.3390/molecules26113467.

Ursachi, V.C., Tanase, C.E., Verestiuc, L., Balan, V., 2023. An explorative study of biotin functionalized magnetic hybrid particles. Mater. Today Commun. 35, 106374. https://doi.org/10.1016/j.mtcomm.2023.106374.

Wang, F., et al., 2011. Synergistic effect of folate-mediated targeting and verapamil-mediated P-gp inhibition with paclitaxel-polymer micelles to overcome multi-drug resistance. Biomaterials 32 (35), 9444–9456. https://doi.org/10.1016/j.biomaterials.2011.08.041.

Wang, W., Xue, C., Mao, X., 2020. Chitosan: Structural modification, biological activity and application. Int. J. Biol. Macromol. 164, 4532–4546. https://doi.org/10.1016/j.ijbiomac.2020.09.042.

Wojcik-Pastuszka, D., Krzak, J., Macikowski, B., Berkowski, R., Osiński, B., Musiał, W., 2019. Evaluation of the release kinetics of a pharmacologically active substance from model intra-articular implants replacing the cruciate ligaments of the knee. Materials 12 (8). https://doi.org/10.3390/ma12081202.

Yang, Y., Teng, P., Yu, S., Meng, Y., Zuo, J., Guo, H., Liu, G., 2025. A review of combined imaging and therapeutic applications based on MNMs. Front. Chem. 13, 1595376. https://doi.org/10.3389/fchem.2025.1595376.

Zhang, E., Xing, R., Liu, S., Li, K., Qin, Y., Yu, H., Li, P., 2019. Vascular targeted chitosan-derived nanoparticles as docetaxel carriers for gastric cancer therapy. Int. J. Biol. Macromol. 126, 662–672. https://doi.org/10.1016/j.ijbiomac.2018.12.262.

Zhao, J., Wu, J., 2006. Preparation and characterization of the fluorescent chitosan nanoparticles probe. Chin. J. Anal. Chem. 34, 1555–1559. https://doi.org/10.1016/S1872-2040(07)60015-2.